Filamented Light (FLight) Biofabrication of Aligned Fibrillar Structures to Direct 3D Cell Organization Within Microgels

Akshat Joshi, Meenakshi Kamaraj, Nafiseh Moghimi, Hossein Heidari,
Arwin Aghamaleky-Sarvestany, Chethikkattuveli Salih Abdul Rahim,
Diego N. Rodriguez-Sanchez, Caroline Hu, Sree Aravindan, Deepthi S. Rajendran Nair,
Ngan F. Huang, Biju B. Thomas, Dhruv Sareen, Eiji Yoshihara, Vadim Jucaud,
Ali Khademhosseini, and Johnson V John*

Controlling cellular organization in hydrogels is of great interest in tissue engineering and regenerative medicine. In the body, cell organization is regulated by aligned extracellular matrices, such as collagen fibers. However, generating patterned extracellular matrix fibers in hydrogels, such as microfabricated gels, is not easily accomplished. Here, filamented-light (FLight)–based 3D microfabrication is used to fabricate microgels with precise internal architecture to direct cellular organization. It is demonstrated that fibrillated rod-shaped microgels encapsulating C2C12 muscle cells promote highly aligned myotube formation, offering potential as mini-injectable muscle tissues for minimally invasive muscle loss therapies. Furthermore, photoreceptor cells encapsulated in rod-shaped microgels generated structures that mimicked the outer retina. Moreover, these microgels can be used as injectable scaffolds, both in vitro and in vivo, where they facilitate angiogenesis when conjugated with QK peptide. Overall, this technique can be used to generate microgels with precise internal architecture thus providing a potentially significant tool for engineering tissue-like structures.

1. Introduction

Hydrogels have been utilized extensively in many biomedical applications, such as in 3D cell culture[1–3] and tissue engineering.[4–6] Despite their biomimetic properties, hydrogels exhibit limitations as injectable materials for cell delivery, primarily due to their nanoporosity, which restricts diffusion and hinders effective tissue infiltration and vascular ingrowth. Thus, microfabricated hydrogels have been increasingly used for tissue engineering as they can be made to have higher surface area-to-volume ratios to enhance cell infiltration and vascular formation after implantation compared to bulk counterparts.

In the body, cells reside in a complex niche that regulates their functions. For example, cellular alignment, which is crucial in various tissues like the heart,

A. Joshi, M. Kamaraj, N. Moghimi, H. Heidari, C. S. A. Rahim,
D. N. Rodriguez-Sanchez, V. Jucaud, A. Khademhosseini, J. V John
Terasaki Institute for Biomedical Innovation
Los Angeles, CA 90024, USA
E-mail: jjohn@terasaki.org
H. Heidari
Institute for Materials Discovery
University College London
London WC1E 6BT, UK
A. Aghamaleky-Sarvestany, D. Sareen
Cedars-Sinai Biomanufacturing Center
West Hollywood, CA 90069, USA
D. N. Rodriguez-Sanchez
Department of Structural and Functional Biology
Laboratory of Nerve Regeneration
Institute of Biology
University of Campinas
SP 13083–862, Brazil

C. Hu, S. Aravindan
Center for Tissue Regeneration
Repair and Restoration
Veterans Affairs Palo Alto Health Care System
Palo Alto, CA 94304, USA
D. S. R. Nair, B. B. Thomas
Department of Ophthalmology
Roski Eye Institute
Keck School of Medicine
University of Southern California
Los Angeles, CA 90033, USA
N. F. Huang
Department of Cardiothoracic Surgery
Stanford University and Veterans Affairs Palo Alto Health Care System
Palo Alto, CA 94304, USA
B. B. Thomas
USC Ginsburg Institute for Biomedical Therapeutics
University of Southern California
Los Angeles, CA 90033, USA
D. Sareen
Board of Governors Regenerative Medicine Institute
Los Angeles, CA 90048, USA

**ADVANCED
SCIENCE NEWS**
www.advancedsciencenews.com

**NANO · MICRO
small**
www.small-journal.com

muscle, and nerve,[7–9] is regulated by extracellular matrix (ECM) fibers. In 2D culture substrates, cells can be induced to align using microarchitectural control, mechanical stimulation, or aligned ECM.[10,11] Control of cellular arrangement in 3D hydrogels is often not well structured due to the isotropic environment for cells. Some control on dictating cellular behavior can be achieved by utilizing microfabricated hydrogels such as microgels, in which cells tend to align within microgels by pulling on their surroundings.[12] However, in these cases the nanofibrous polymers are often randomly oriented with no inherent anisotropic properties.[13]

Material anisotropic properties in hydrogels can be generated by aligning polymer networks inside the hydrogels.[14] Conventional approaches such as strain-induced cellular alignment,[15,16] fiber-reinforced cellular alignment,[17] utilization of anisotropic gel,[18] and other external stimulation-driven approaches[19] have been used to direct cellular response in a 3D environment. However, such methodologies are complex and not scalable. Shape-induced anisotropy in microgels can be achieved using microfluidics, however the control of such alignment is limited.[20,21] Recently, microgel-based granular hydrogels have garnered significant attention for their potential in tissue repair and regeneration applications.[22,23] The majority of microgels have been synthesized using techniques such as microfluidics,[24,25] emulsion processes,[26] and fragmentation methods.[27] However, these approaches have notable limitations, particularly in their inability to control or influence the internal architecture of the microgels. In this study, we aim to overcome these challenges by utilizing Filamented Light (FLight) biofabrication, a novel technique that enables the precise organization of cellular alignment within the microgels.

Recently deep vat photopolymerization (DVP) 3D printing approaches have gained much attention in 3D biofabrication. DVP techniques such as volumetric bioprinting[28,29] have allowed researchers to create complex millimeter-scale tissue architectures within a fraction of a seconds with uncompromised cellular viability. Similarly, FLight biofabrication has been shown to generate millimeter-scale anisotropic hydrogel constructs that can provide filamentous niches to control cellular arrangement.[30–32] Although these techniques have gone a long way in resolving many issues associated with light-based biofabrication techniques, they often are designed for macroscale constructs with their minimal utilization for fabricating microgels. Although some recent research have explored the potential of light-based biofabrication at the microscale,[33] the technique was unable to generate microparticles with anisotropies. Considering the need to direct cellular response in microgels and to incorporate various designs

D. Sareen
Department of Biomedical Sciences
Cedars-Sinai Medical Center
Los Angeles, CA 90048, USA

E. Yoshihara
The Lundquist Institute for Biomedical Innovation at Harbor-UCLA
Medical Center
Torrance, CA 90502, USA

E. Yoshihara
David Geffen School of Medicine at University of California Los Angeles
Los Angeles, CA 90095, USA

of modular scaffolds, here, we aim to use the FLight microfabrication technique to fabricate nonspherical microgels with internal anisotropy. The study demonstrates that FLight can be used to make anisotropic microgels. Our newly developed system can engineer anisotropic microgels with precise cellular organization inside the microgel and their assemblies at microscales that can be used for diverse tissue engineering applications. We believe the developed fabrication modality can be utilized as a new approach for microgel synthesis and their unique assemblies.

2. Results and Discussion

Microgels were fabricated using gelatin methacryloyl (GelMA, degree of methacrylation 75%)/polyethylene glycol diacrylate (PEGDA, Mn 750 Da) based photoactive resins wherein the fraction of two components were varied to prepare gels of different stiffnesses. We used a customized 2D projector system to focus collimated light beam of designed geometries using a digital micromirror device (DMD) onto a photoactive resin. The concept is based on the OMI of the uniform light beam as it passes through a nonlinear medium, breaking it into microfilaments.[32] This can result in macroscale constructs that are highly filamentous and can be utilized to control cellular arrangements in 3D. We hypothesized that such behavior of light could be used in making internal fibrillation in microgels (**Scheme 1**).

Initially, we demonstrated the ability of our approach to fabricate microgels of varying chemistries, shapes, and sizes ranging from 300 to 900 μm with a range of photoresin formulations, as shown in **Figure 1A**i–iii. Different photoresins were utilized composed of GelMA (7.5% w/v, G7.5) or GelMA blended with varying concentrations of PEGDA (P2.5G7.5, P5G7.5, where numbers represent w/v concentration of each polymer). We demonstrated that these formulations have mechanical properties that ranged from 10–50 kPa (Figure 1B,C), allowing us to target tissues of varying stiffnesses. Moreover, we confirmed that these microgels were injectable, envisioning their applications for minimally invasive therapeutics (Figure 1D; Figure S1, Supporting Information).

We subsequently investigated the degree and pattern of fibrillation in microgels synthesized from various pre-polymer concentrations (Figures S2 and S3, Supporting Information). Our observations revealed that microgels with a low aspect ratio (shapes such as square, star, and triangle) lacked filamentous structures, while those with a high aspect ratio, such as rod-shaped microgels, exhibited an internal fibrillated architecture. This could be probably due to the depth of penetration of light in photoresins, with deeper penetration enhancing the waveguiding effects (as observed in the case of high aspect ratio microgels such as rods) whereas the phenomenon could be greatly suppressed when the penetration depth was lesser (as in the case with flattened microgels such as squares, triangles, and any other 2D shapes). Cross-sectional analyses of the higher aspect ratio microgels revealed a dotted grid-like arrangement of filaments, with microchannels interspersed throughout. Conversely, the microgels with lower aspect ratios displayed a smooth architecture, indicating the absence of fibrillation (Figure S3, Supporting Information). We also collected additional Z-stack images to analyze the filament arrangement within microgels of high aspect ratios fabricated using different pre-polymer compositions, to analyze the role of
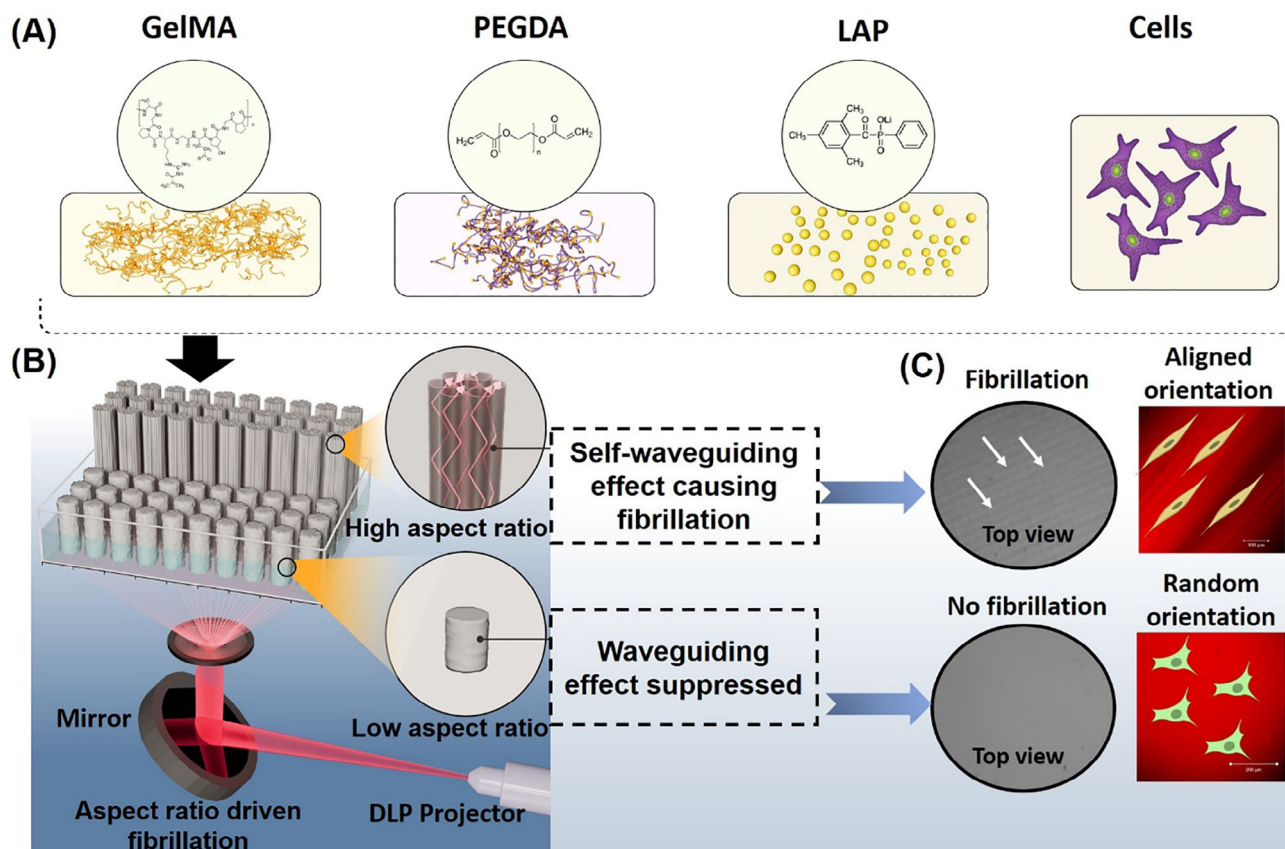
Scheme 1. FLight-based fabrication of microgels with fibrillar architecture. A) Bioink composed of varying concentrations of GelMA/PEGDA as a precursor can be used to fabricate microgels. B) The customized DMD setup can selectively fabricate microgels of different shapes with or without fibrillar architecture based on optical modulation instability (OMI). C) Fibrillation of microgels can control cellular arrangement in 3D.

polymer composition in controlling fibrillation. All formulations displayed an internal filamentous architecture with interspersed microchannels. Notably, reducing the PEGDA concentration resulted in an increase in both the diameter of the filaments and the size of the corresponding microchannels (Figure S4, Supporting Information).

Cellular arrangement is an important factor that can modulate tissue functionality.[34,35] We demonstrated the capability of our biofabricated microgels to influence cellular alignment (**Figure** 2A; Figure S5, Supporting Information). We hypothesized that the internal fibrillation in elongated geometries, such as rods, offers directional cues for cell alignment, while the absence of fibrillation in low aspect ratio geometries, like square modules, leads to random organization of cells. We fabricated microgels encapsulating human dermal fibroblasts (HDFs) with varying aspect ratios—rods representing high aspect ratio geometries (≈ 500 µm) and squares representing low aspect ratio geometries (≈ 500 µm) to assess cellular arrangement over time. Live/dead staining results (Figure 2B) showed that cells remained viable within both rod and square microgels. However, the organization of the cells differed between the two microgel types. Cells within rod-shaped microgels exhibited alignment over five days (Figure 2Bi), while those in square-shaped microgels maintained a random orientation (Figure 2Bii). The Alamar Blue assay conducted over five days indicated a significant increase in

metabolic activity ($^{****}p < 0.0001$) (Figure 2C), confirming the absence of toxicity from the bioink formulation and light exposure during fabrication. Importantly, the observed cellular alignment was attributed solely to internal fibrillation, rather than the external architecture of the microgels (Figure S6, Supporting Information). High-resolution confocal imaging of the cytoskeleton further illustrated the ability of our fabricated micro-units to regulate cellular arrangement at the microscale (Figure 2D; Figure S7, Supporting Information). Thus, our findings support the hypothesis that the newly developed microgel system is not only anisotropic in shape but also features an internal architecture that can be tailored to modulate cellular arrangements in various configurations.

Next, we tested the utility of FLight-based microgels in fabricating anisotropic tissues like muscle.[36,37] Although microgels have been researched recently as injectable cell carriers for the treatment of volumetric muscle loss,[38,39] the isotropic nature of such systems restricts their potential for efficient cell-based therapies. Given that our FLight microgels with fibrillation can provide directional cues, we envisioned their use as cell-laden injectable microfillers in regenerative medicine (Figure 3A). We fabricated rod-shaped microgels ≈300 µm in diameter and assessed their potential to align muscle cells. As demonstrated (Figure 3B), there was no observed impact on cell metabolic activity following injection. Cells demonstrated an increase in
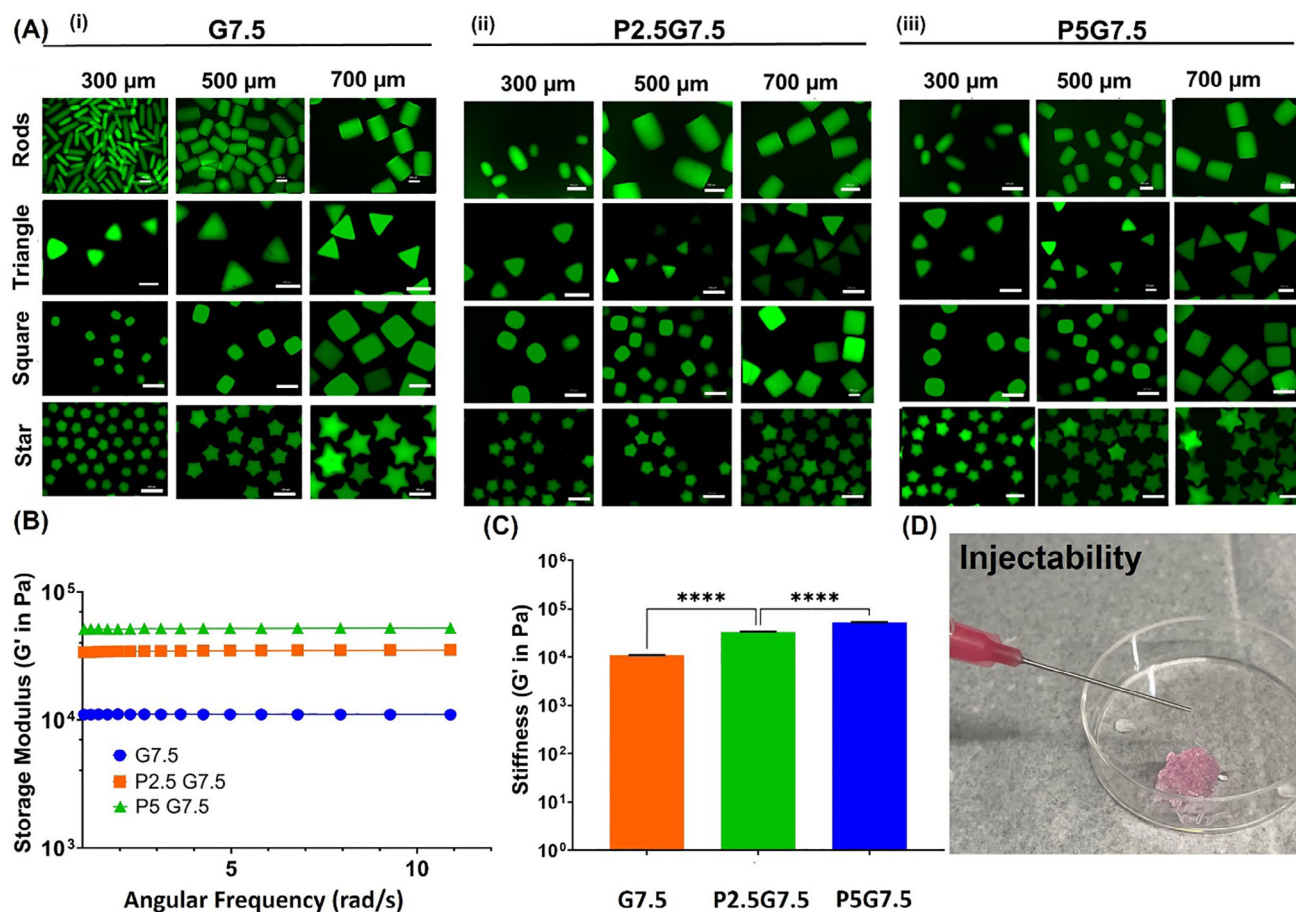
Figure 1. FLight-based fabrication of microgels. A) Different microgel shapes were fabricated using different hydrogel compositions. (i) GelMA 7.5%, (ii) PEGDA2.5% / GelMA 7.5%, (iii) PEGDA 5% / GelMA7.5%. B) Frequency sweep analysis of different hydrogel compositions demonstrating different storage moduli. C) Stiffness of different hydrogel compositions. D) Injectability of fabricated microgels through a 21G needle. *Scale bars*: 500 µm, $^{****}p < 0.0001$.

metabolic activity over 7 days ($^{****}p < 0.0001$), with no significant differences noted before and after injection. Live/dead staining confirmed that cells remained viable and aligned throughout 5 days of culture (Figure 3Ci,ii; Figure S8, Supporting Information), with no visible effects of injection on cell viability or organization. Cytoskeleton staining (Figure 3Di,ii; Figure S8, Supporting Information) indicated that cells began to align by day 1 and populated the microgels over 5 days, with fused cytoskeleton structures observed at day 5. We did not detect any adverse effects of injection on the arrangement of the cytoskeleton (Figure 3Di,ii; Figure S9, Supporting Information).

Moreover, the advantages of FLight microgels were highlighted by their ability to support muscle maturation. Following cell fusion observed in cytoskeleton staining, cells were cultured for another 7 days in induction media, to induce muscle formation and maturation. To confirm the commitment of cells toward myogenesis, Desmin staining was conducted, specifically 4 days post-induction in differentiation media (early time point). The results revealed a significant number of cells that tested positive for Desmin, indicating their differentiation toward the muscle lineage (Figure S10, Supporting Information). By day 7 following induction, FLight microgels exhibited remarkable effectiveness
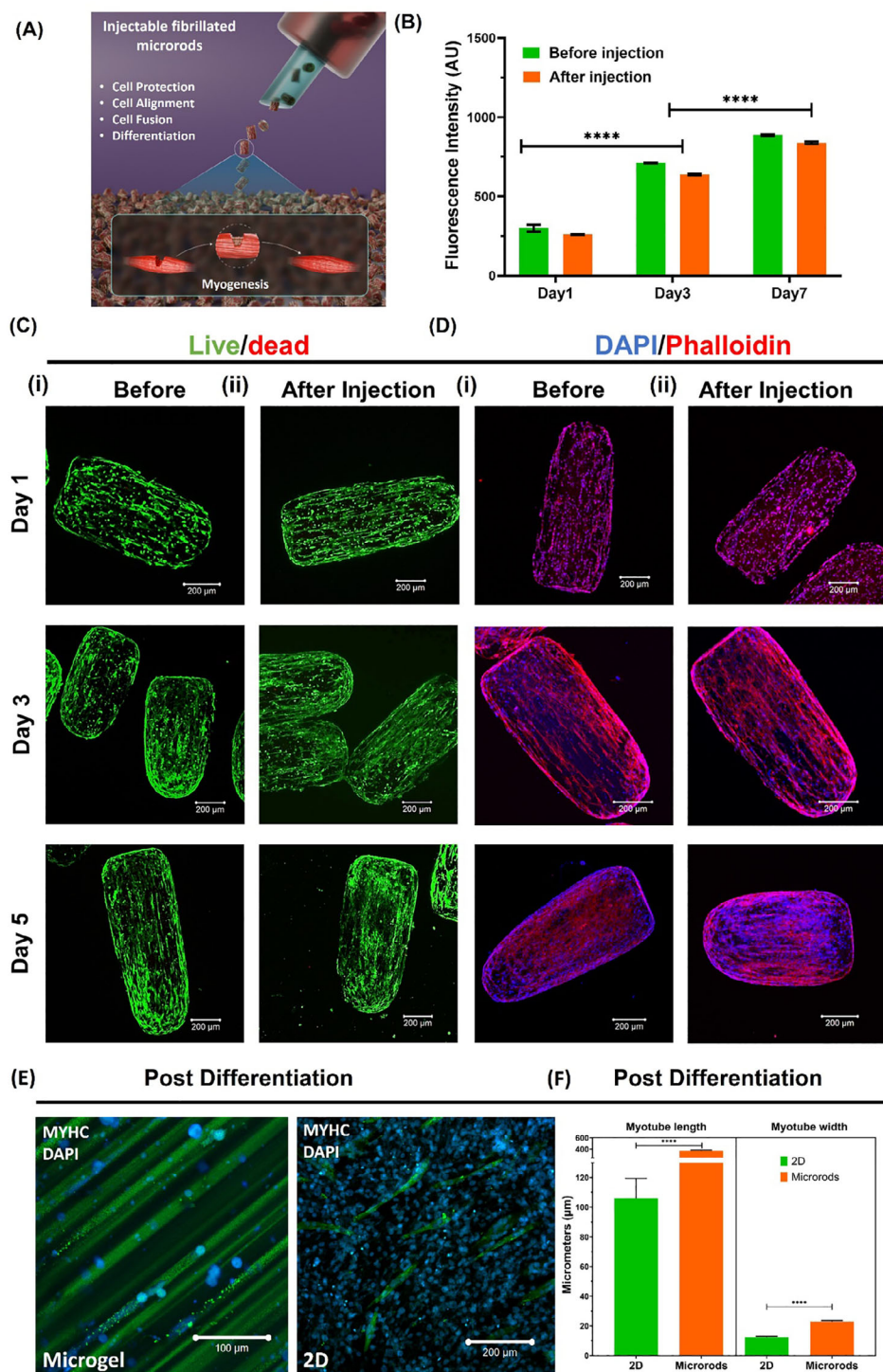
in promoting cell differentiation, leading to the development of highly aligned myotubes within the microgel (Figure 3E; Figure S11, Supporting Information). In contrast, cultures maintained in 2D environments showed significantly less successful differentiation, largely due to their inability to facilitate the directional growth of the cells.

Further quantitative analysis of myotube parameters—such as their length and width, as depicted in Figure 3F—reinforced the superior capability of FLight microgels in fostering positive cellular responses. These findings underscore the importance of the 3D architecture provided by the microgels, which effectively mimics the natural extracellular environment. This environment is essential for supporting the complex interactions and alignment that drive optimal muscle cell development, ultimately enhancing the functionality and maturity of the engineered muscle tissue.

To assess the effectiveness of FLight-based biofabrication in replicating the intricate cellular structures typically found in tissues such as the retina, we fabricated a Janus-type assembly (**Figure 4A**), wherein photoreceptors (PRs) loaded fibrillated microrods were biofabricated on top of GelMA membranes that contained a confluent monolayer of retinal pigment epithelial

ADVANCED
SCIENCE NEWS

www.advancedsciencenews.com

NANO · MICRO

small

www.small-journal.com
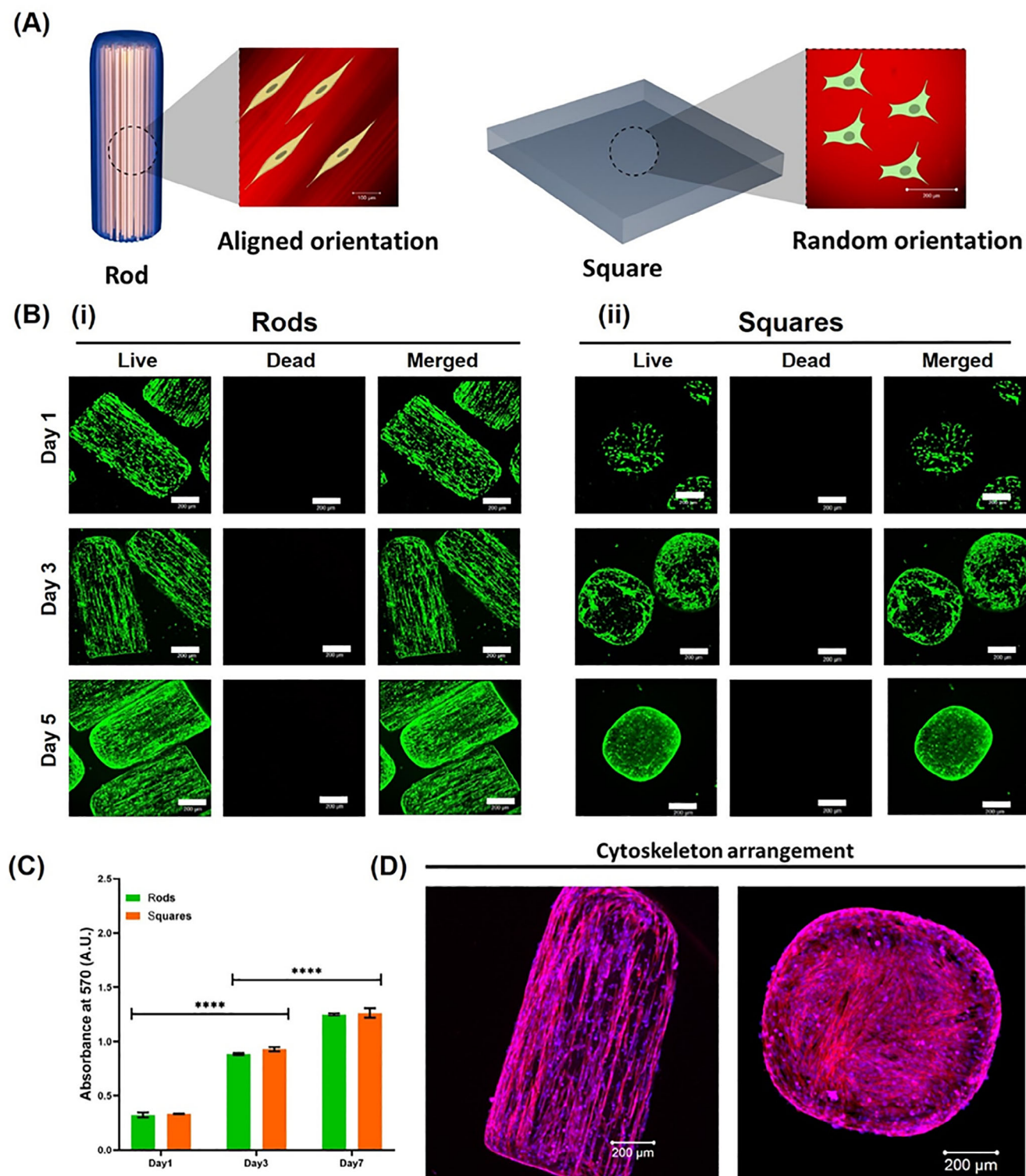
Figure 2. Biofabricated microgels can impact the cellular organization by controlling OMI. A) Schematic representation demonstrating how OMI can be modulated to control cellular arrangement in microgels of different shapes by controlling internal architecture. B) Live-dead staining showed high cellular viability of HDF cells over 5 days with (i) microrods providing an elongated cellular arrangement due to their fibrillar architectures inside the microgels, whereas (ii) cells organized randomly in square-shaped microgels. C) Presto blue assay demonstrating cellular growth in both shapes over 7 days. D) High-magnification staining for cytoskeleton (Phalloidin staining) demonstrating how internal structures can impact cellular arrangement in microgels. *Scale bars*: 200 µm, [****] $p < 0.0001$.

ADVANCED
SCIENCE NEWS

www.advancedsciencenews.com

NANO · MICRO

small

www.small-journal.com

Figure 3. Fibrillated rods can provide guided cellular growth. A) Schematic illustration demonstrating the possible application of fibrillated microgels for cell-based therapeutics, wherein microgels can help in a cellular organization that can be utilized as fillers for the treatment of muscle loss. B) Metabolic activity of C2C12 cells encapsulated in microgels before and post-injection. No significant difference was observed in metabolic activity post-injection. C) Live/dead staining demonstrating high cellular viability and cell alignment during 5 days of culture. (i) Before injection, (ii) After injection. No impact on cellular viability nor cellular alignment was observed post-injection. D) Phalloidin/DAPI staining showing the alignment of the cytoskeleton on microgels. (i) Before injection, (ii) After injection. No impact on cellular alignment was observed post-injection (*Scale bar*: 200 μm). E) Microgels stained positive for Myosin after 7 days of culture in differentiation media (*Scale bar*: 100 μm). Prior to switching to differentiation media, the microgels were cultured in growth media for 7 days, followed by an additional 7 days of induction. While cells in 2D cultures exhibited some capacity for differentiation, their effectiveness was notably inferior compared to the 3D culture in FLight microgels (*Scale bar*: 200 μm). F) Quantitative assessments of myotube length and thickness. [****] $p < 0.0001$.
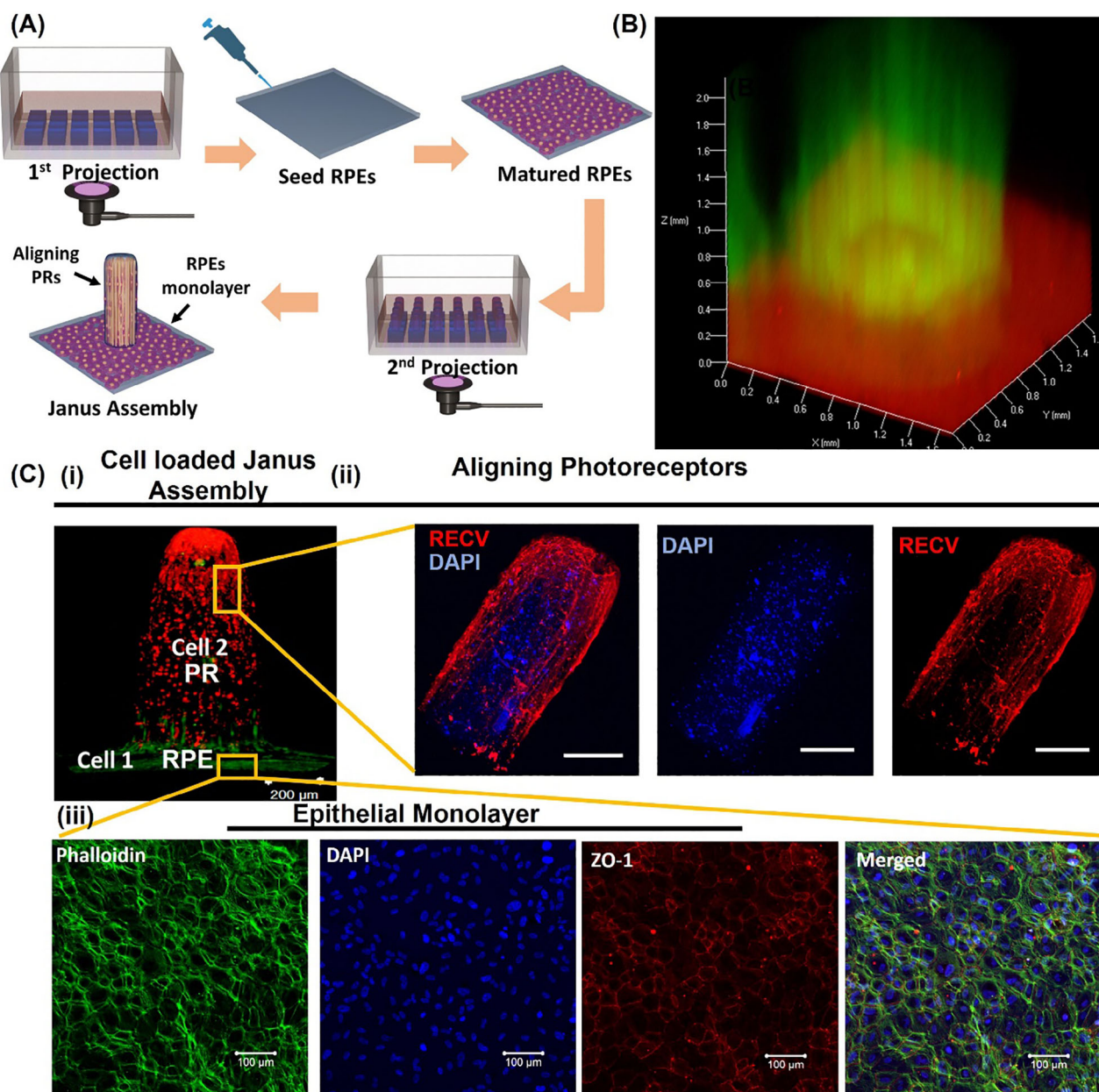
Figure 4. Janus-type modular assembly mimicking physiology of retina. A) Schematic representation showing fabrication of Janus-type units with the capacity to control cellular arrangements. Epithelial monolayer (RPEs) surrounding the pillar of Janus Assembly loaded with photoreceptors (PRs) can mimic the physiology of cellular arrangement in the retina. B) Microscopic observation of Janus Type assembly showing fibrillated pillars biofabricated on GelMA membranes. C) Cell-loaded Janus-type assembly. (i) Tracked cells loaded in two regions of Janus type assembly (*Scale bar*: 200 μm), (ii, iii) IF staining demonstrating cells positive for ZO-1 (Red: ZO-1, Blue: Nuclei, Green: Phalloidin; *Scale bars*: 100 μm) and recoverin (Red: Recoverin, Blue: Nuclei, *Scale bars*: 200 μm) respectively in base and pillars of Janus Assembly.

(RPE) cells. These assemblies can replicate the retinal structure, with such cellular arrangements being crucial for ensuring proper functionality.[40] Microscopic analysis of the Janus-type assembly (Figure 4B) reveals filamentous microrods biofabricated atop GelMA membranes. To delineate distinct cell-laden regions within the Janus-type assembly, cells were labeled with green and red fluorescence trackers (Figure 4Ci). Initially, RPE-seeded GelMA membranes were observed for 14 days to verify the formation of a viable monolayer of RPEs (Figure S12, Sup-

porting Information). Subsequently, the RPEs were cultured for an additional 7 days to promote the maturation of the established monolayer. Following this maturation period, photoreceptor-loaded fibrillated rods were biofabricated on top of the GelMA membranes containing the matured RPE monolayer. Observation of the microrods indicated that PRs could align and sustain high viability over a 7-day culture period (Figure S13, Supporting Information). Immunofluorescence staining on day 7 further demonstrated that encapsulated PRs retained expression of

**ADVANCED
SCIENCE NEWS**

www.advancedsciencenews.com

**NANO · MICRO
small**

www.small-journal.com

Recoverin, a phototransduction-related protein (Figure 4Cii). Additionally, base-level microscopic analysis revealed a monolayer of RPEs with tight junction formation, as evidenced by immunofluorescence staining for ZO-1 (Figure 4Ciii). These Janus-type microtissue constructs have potential applications in tissue engineering and regenerative medicine. Specifically, the fabricated retina-mimicking assembly could be employed in the treatment of age-related macular degeneration, with PR-loaded assemblies and supportive RPEs potentially serving as implantable microtissues.

We further explored the adaptability of our fabrication system by configuring these modules into various setups to recreate microtissue-like assemblies. In the body, tissues typically possess a well-organized vascular pattern essential for their function and development. While many studies have shown that co-culture models can accelerate the anastomosis process, most have struggled to control or pattern these cellular arrangements effectively.[41,42] Moreover, these studies did not consider that tissues are a collation of micromodules connected through a well-organized vasculature. To illustrate this, we created a modular microgel sheet featuring an array of microsquares interconnected by perfusable microchannels (Supplementary Video V1). As demonstrated (Figure S14A, Supporting Information), we hypothesized that these microchannel-embedded sheets could be used to culture human donor-derived endothelial cells selectively within the channels. This would result in scaffolds with patterned, well-organized vascular networks around the micromodules, suitable for housing tissue-specific cells. Figure S14Bi,ii presents both the macroscopic and microscopic views of the micro-modular assembly, highlighting the connection of microsquares and the presence of microchannels. We investigated the potential of these micro-modular units for creating patterned cellular arrangements. Endothelial cells derived from induced pluripotent stem cells (iECs) seeded onto the micro-modular scaffolds, as shown in Figure S14Ci,ii demonstrated their ability to confine themselves to the channels. By day 7, these cells formed a well-defined patterned architecture with high viability and significant expression of the canonical vascular endothelial cell marker CD31/PECAM-1 (Platelet Endothelial Cell Adhesion Molecule-1). These micro-modular hydrogel sheets effectively replicate the arrangement of micro-units connected by vasculature, akin to the structure found in native tissues.

Next, we assessed the capacity of microgels to support host tissue growth and vascularization when employed as injectable materials. To demonstrate this, we utilized microgel assemblies, referred to as microporous scaffolds (MAPs), which exhibited distinct in vitro and in vivo cellular infiltration patterns that were influenced by the geometry of the microgels. In vitro, we annealed square- and rod-shaped microgels into MAPs and evaluated the impact of microgel shape on cellular infiltration. While MAPs made from square and rod-shaped microgels exhibited similar overall porosity, their internal 2D architecture differed, with square-based MAPs displaying a higher degree of pore interconnectivity compared to rod-based MAPs (**Figure 5**Ai,ii). Mechanical property analysis revealed significant differences in storage modulus (G′) between the two MAP types ($^*p < 0.05$) (Figure 5A-iii; Figure S15, Supporting Information). This variation in pore structure and mechanical stiffness influences cellular infiltration. To test this hypothesis, human dermal fibroblasts

(HDFs) were cultured on the MAPs, and cell growth and infiltration were monitored for 5 days. Cell confluence increased on both MAP types from day 1 to day 5, with cells infiltrating the pores (Figure 5Bi,ii). Volumetric Z-stack images confirmed that cells began infiltrating both MAPs from day 1, with peak infiltration observed by day 5 (Figure S16, Supporting Information). However, the depth of infiltration was shape-dependent, with significantly greater infiltration occurring in square-based MAPs compared to rod-based ones ($^{****}p < 0.0001$) (Figure 5C,D). Overall, we demonstrated that regardless of the particle shape, both types of assemblies enabled efficient cell growth and infiltration, owing to their porous architecture. These findings are crucial for understanding the potential of such injectable assemblies to support cellular infiltration, highlighting their advantage over traditional bulk hydrogels.

Further, we conducted subcutaneous implantation of square- and rod-shaped microgel plugs in a mouse model. To enhance the therapeutic potential of the microgels, they were loaded with QK peptide, an angiogenic factor known to promote angiogenesis.[43,44] The study involved four experimental groups (**Figure 6**A): Rods and Squares, each with and without QK peptide (200 µL of each microgel plug), where QK- represents microgels without peptide and QK+ denotes those loaded with the angiogenic peptide (500 µg mL^{-1} of microgel). Histological analysis at 14 days post-injection revealed that both microgel plugs facilitated cellular infiltration and neo-vascularization at the implantation site due to their microporous architecture (Figure 6Bi–iv). Notably, peptide-loaded microgels exhibited a more pronounced effects, with square-shaped microgels showing a significantly greater degree of infiltration and neo-vessel formation compared to rod-shaped microgels ($^{**}p < 0.01$) (Figure 6B,C). This finding aligns with our in vitro results, suggesting that microgels allowed cellular infiltration because of an interconnected pore network. Also, the results can infer the importance of pore interconnectivity in governing the phenomenon of cellular migration, giving our technique an edge to fabricate microgels of unique shapes and sizes. While the internal architectures can well control the arrangement of the loaded cells, external structures can provide a diverse range of porosities, thus allowing us to control cellular response to a greater extent.

Immunofluorescence staining for CD31, a marker for endothelial cells, was performed to assess new vessel formation. The CD31-stained tissue sections (Figure 6Di–iv) indicated that peptide-loaded microgels stimulated greater vessel formation compared to non-peptide-loaded microgels, with squares showing superior vascularization compared to rods. This underscores the significant role of microgel shape in promoting neo-tissue growth and vascularization. Quantitative analysis of new vessel formation and CD31$^+$ cell counts further supported these observations, showing significantly enhanced neo-vascularization in peptide-loaded microgels (Figure 6E,F; $^*p < 0.05$) and notably more in square-shaped microgels compared to rod-shaped ones (Figure 6E,F; $^{***}p < 0.0002$ for neo-vessels and $^{****}p < 0.0001$ for CD31+ cells).

Overall, our study demonstrates that microgels can effectively support tissue regeneration and neo-vascularization, with microgel shape playing a crucial role in their performance. By modifying the shape of microgels, the scaffold's ability to promote tissue growth and vascularization can be optimized, allowing for
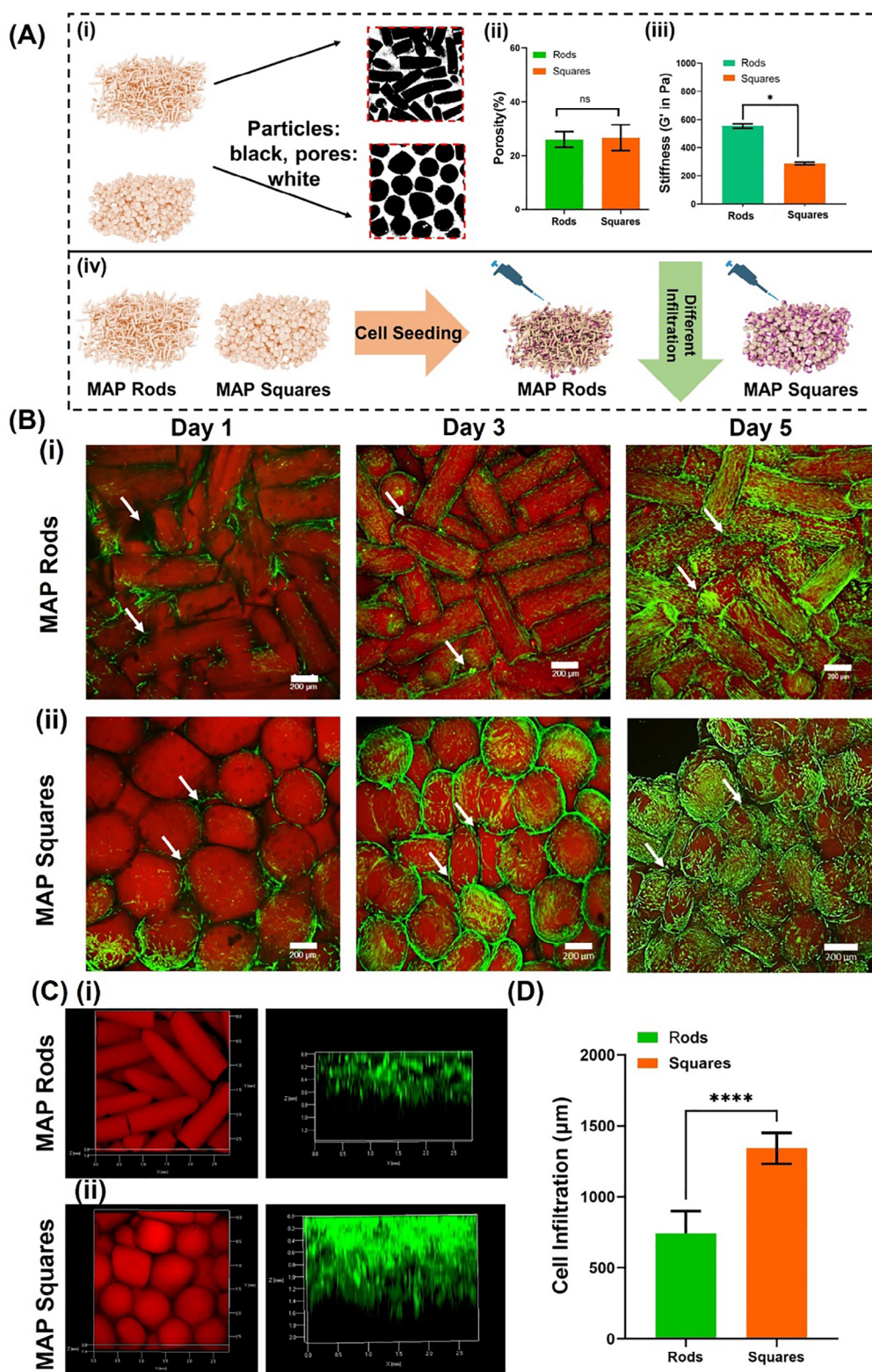
Figure 5. Anisotropic MAPs can be fabricated using nonspherical microgels. A) (i-iii) MAP composed of rods and squares showing different internal architecture, micro-porous architecture, and different stiffness; (iv) Schematic representation demonstrating cells infiltrating MAPs. B) HDF cells cultured on MAPs over 5 days. (i) MAP rods, (ii) MAP squares. Cell proliferated over 5 days in both MAPs and infiltrated the micro-pores (white arrows). Red: Microgels, Green: FITC tracked cells. *Scale bars*: 200 μm. C) (i) 3D image of rod-shaped MAP and respective cell infiltration; (ii) 3D image of square-shaped MAP and respective cell infiltration; D) Comparison of cell infiltration within both MAPs. *Scale bars*: 200 μm. $^*p < 0.05$, $^{****}p < 0.0001$.
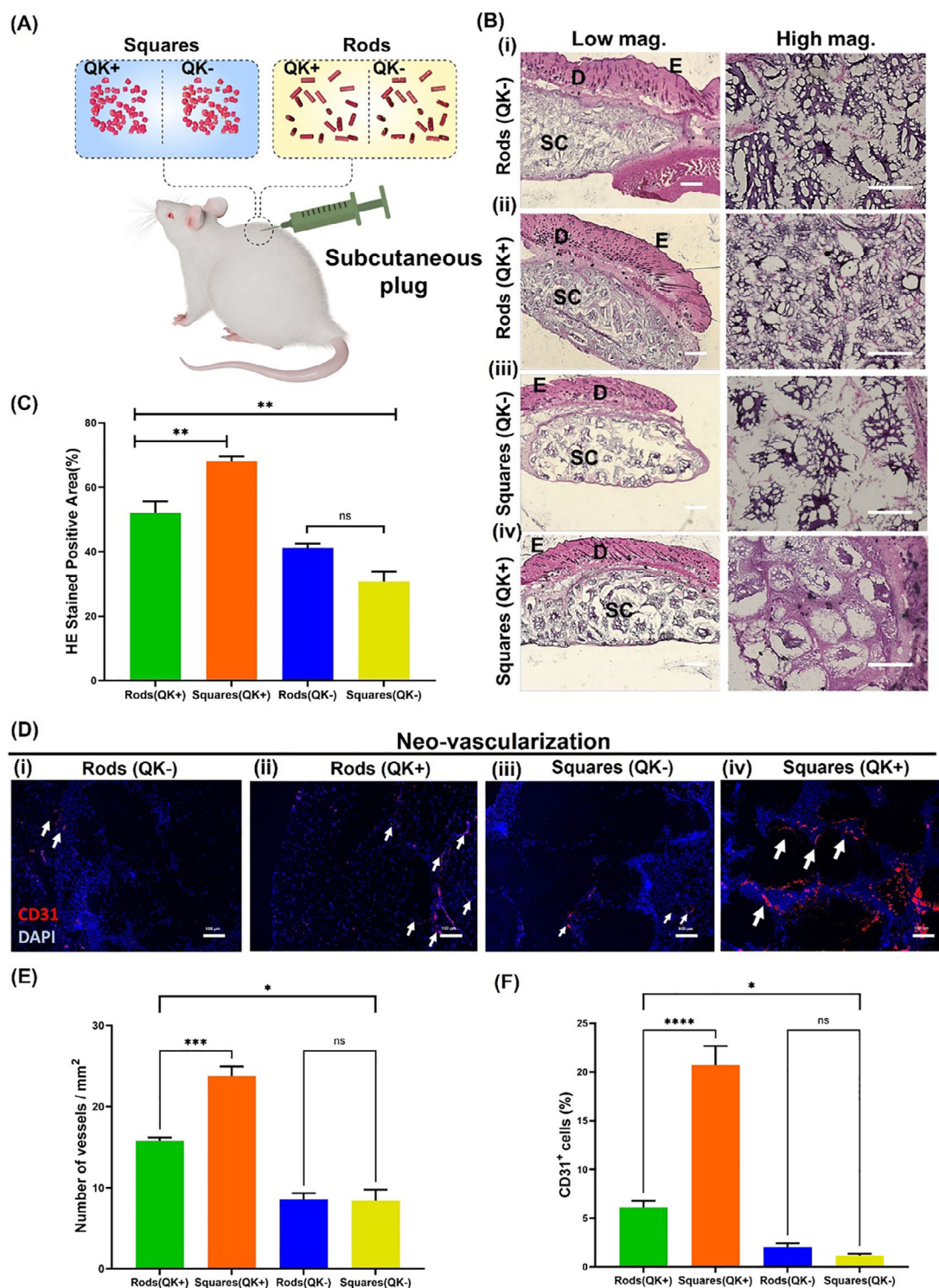
Figure 6. Subcutaneous implantation of microgels in a mouse model. Both microgels (rods and squares) were loaded with QK (angiogenic peptide) to evaluate their angiogenic potential and neo-tissue formation. A) Schematic representation demonstrating the process. 200 µL of each shape was administered using a 21G needle. B) H & E staining demonstrating tissue infiltration through micro-pores of injected microgel plug post 14 days of implantation. (i) Microrods without QK peptide, (ii) Microrods with QK peptide, (iii) Microsquares without QK peptide, (iv) Microsquares with QK peptide. *Scale bars*: 500 µm. C) Quantified tissue infiltration. D) Neo-vascularization at the implantation site. i) Microrods without QK peptide, (ii) Microrods with QK peptide, (iii) Microsquares without QK peptide, (iv) Microsquares with QK peptide. Peptide loading enhanced the process of new vessel formation. Arrows represent newly formed vessels stained positive for CD31. *Scale bars*:100 µm. E) Quantified vessels. F) Quantified CD31+ cells. E: Epidermis, D: Dermis, SC: Subcutaneous cavity. $^*p < 0.05$, $^{**}p < 0.01$ $^{***}p < 0.0002$, $^{****}p < 0.0001$.

**ADVANCED
SCIENCE NEWS**

www.advancedsciencenews.com

NANO · MICRO

small

www.small-journal.com

tailored responses depending on the specific tissue and extent of new tissue formation required.

3. Conclusion

We developed a FLight-based microfabrication technique for creating anisotropic microgels that can effectively influence cellular behavior. By tuning the OMI of light during its interaction with hydrogels, we demonstrated that we can modify the internal structure of these microgels. This innovative approach allows for the design of microgels with tailored internal architectures that can steer a cellular organization in 3D space. Our research illustrates how this precise control over cellular behavior can address the complexities found in various tissues, including muscle and retinal tissues. The injectability of these microgels, combined with their ability to regulate cellular arrangement, positions them as promising tools for regenerative medicine applications. In essence, this microfabrication method paves the way for the development of modular tissue engineering platforms. By enabling the production of anisotropic microgels, our approach holds significant potential for advancing regenerative therapies. These tailored microgels could lead to more effective treatments by providing an environment that closely mimics the native tissue architecture and functionality, ultimately enhancing tissue repair and regeneration. By tailoring the polymer compositions and minimizing light scattering for photo resins loaded with high cell density/organoids,[45] the technique can be further employed to generate microgels with high cellular densities, further exploring its potential to develop complex micro-niches mimicking in vivo physiologies.

4. Experimental Section

Synthesis of GelMA: GelMA was synthesized as reported previously.[46,47] Briefly, 10 gm of Gelatin Type A (Sigma–Aldrich) was dissolved in carbonate buffer (pH: 9.0) at 40 °C under constant magnetic stirring. Following complete dissolution after 2 h, methacrylic anhydride (1 mL, Sigma–Aldrich) was added gradually, and the reaction was allowed to proceed for 4 h. The reaction was terminated by adjusting the pH to 7.0, and the solution underwent dialysis for 3 days using a 14 kDa dialysis membrane, with water changes occurring every 12 h. Subsequently, the solution was lyophilized for 2 days to yield GelMA flakes, which were stored at −20 °C for future applications. The degree of functionalization (DoF) was quantified using a Ninhydrin assay.[48] (Figure S17, Supporting Information).

Preparation of Photoresins: Photoresins were formulated using either pure GelMA (7.5% w/v) or by blending GelMA with varying concentrations of PEGDA (Mn 750 Da, Sigma–Aldrich). Specifically, GelMA, PEGDA, and 0.1% Lithium phenyl-2,4,6-trimethylbenzoylphosphinate (LAP, Sigma–Aldrich) were dissolved in PBS at 40 °C for 30 min to achieve a homogeneous solution. Three distinct types of photoresins were prepared for the fabrication of microgels: GelMA at 7.5% w/v; GelMA at 7.5% w/v combined with PEGDA at 2.5% w/v (denoted as P2.5G7.5); and GelMA at 7.5% w/v combined with PEGDA at 5% w/v (denoted as P5G7.5).

FLight Based Fabrication of Microgels: Microgels were fabricated using a FLight setup that transmitted 405 nm light from an LED to a Texas Instruments DMD (Light Crafter 4500), illuminating a cubic vial (51 mm × 51 mm) filled with photoactive resins using various geometrical light patterns, achieving a maximum irradiance of 20–25 mW cm^{-2} at the image plane. Different microgel shapes were designed using a greyscale format, where each shape corresponds to 100% light intensity. The designed images were converted to JPEG format for projection. The photoactive resins

were poured into cubic vials and maintained at 4 °C to allow thermal gelation, after which they were placed on the print platform where the projector selectively cross-linked the resin at specific locations, forming distinct microgel shapes. This thermal gelation facilitated high OMI, enabling the formation of fibrillated structures. After 50 s of exposure, the cubic vials were stored at 37 °C to reverse thermal gelation and to remove uncross-linked photoactive resin, with microgels collected using a 100 µm cell strainer for subsequent processing. For fabrication with cells (1.5 million mL^{-1} of photoresin), all protocols were conducted in a sterile environment, and the photoresin was mixed with cells prior to being placed in the cubic vial. A 7.5% GelMA-based bioink was employed for all cell-related experiments.

Rheological Evaluation of Photo Resins: For rheological analysis, photoresin discs (8 mm diameter, 1 mm thickness) were fabricated using FLight. Rheological properties were evaluated using frequency sweep analysis between 0.1 to 10 Hz at 1 mm plate gapping using MCR Anton Paar. G′ values were utilized for stiffness calculations.

Injectability Evaluation: To assess the injectability of the microgels, microgels measuring ≈500 µm were fabricated and collected using a cell strainer. The collected microgels were then transferred into a 5 mL syringe and injected through a 21G blunt nozzle. To visualize the microgels within the channel, transparent 21G glass channels were employed, and images were captured using a fluorescent microscope (Keyence Inverted Fluorescence Microscope, Trinocular, Halogen Light).

Fabrication of MAPs: For fabrication of MAPs, collected microgels (rods and squares) were resuspended in 0.1% LAP solution, centrifuged at 10 000 rpm for packing, and placed in Polydimethylsiloxane (PDMS) molds (2 mm thick, 8 mm diameter). They were further stabilized by exposure to 405 nm light, and the fabricated MAP discs were then utilized for cell seeding. All procedures were performed in a sterile environment. Rhodamine solution (0.01%) was used for microgel fabrication for their easy observation under a confocal microscope.

MAP Characterization: MAP discs were synthesized to evaluate the stiffness of MAPs composed of rods and squares, as stated above. Rheological properties were evaluated using frequency sweep analysis between 0.1 to 10 Hz at 1 mm plate gapping using an MCR Anton Paar Plate rheometer. G′ values were utilized for stiffness calculations. For porosity calculation, 2D slices from z-stacked images were obtained and the porosity was calculated as reported previously.[20] For cell infiltration in MAPs, cell-seeded MAPs (microgels tracked with FITC, HDF cells tracked green, 20 000 cells/ MAP disc) were imaged at different time points. 3D images were used to calculate the depth of penetration. At each time point, at least 3 samples were imaged, and at least 3 independent experiments were performed.

Fabrication of Modular Hydrogel Sheets: To fabricate modular hydrogel sheets, a design consisting of microsquares (≈500 µm) was initially created in greyscale format. The spacing between adjacent microsquares was maintained at 200–400 µm, resulting in microchannels of similar dimensions. GelMA photoresins were poured into rectangular vials and kept at 4 °C to promote physical gelation. The vials were then exposed to a FLight setup to selectively cross-link the projected micro-areas, yielding hydrogel sheets. After exposure, the embedded hydrogel sheets were retrieved by melting the photoresin at 37 °C for 10 min. The resulting sheets were thoroughly washed with PBS and stored for future use.

For seeding iECs onto modular scaffolds, on Day 11 of the experiment, iECs were gently added in a drop-wise manner at a density of 100 000 cells per 10 mL in an iEC differentiation medium. After a 30-min incubation, the plate was filled with additional differentiation medium. The iECs were fed every other day, and cell analysis was conducted on Days 3 and 7 post-seeding. The viability of the iECs was assessed using the LIVE/DEAD Viability/Cytotoxicity Kit (Thermo Fisher Scientific), which differentiates between live and dead cells. Live cells were identified by green fluorescence from Calcein-AM, while red fluorescence from ethidium homodimer-1 indicated cell death.

To characterize the seeded cells, immunostaining was performed. The iECs were first fixed with 4% paraformaldehyde. After washing with PBS, the cells were blocked and permeabilized in a PBS/0.1% Triton-X (Bio-Rad) and donkey serum (Millipore) solution for 1 h at room temperature. Immunostaining was carried out using antibodies against the endothelial

marker CD31 (Cell Signaling) at a dilution of 1:100 for 1 h at room temperature. Following thorough washing with 0.1% Tween 20 (Thermo Fisher) in PBS, the cells were incubated with secondary antibodies targeting mouse (excitation wavelength 647) for 1 h at room temperature. Finally, the cell nuclei were stained with DAPI.

Fabrication of Janus Assembly: GelMA membranes were initially fabricated using the FLight technique and subsequently seeded with RPEs at a density of 2700 cells per membrane. These membranes were cultured for 14 days to develop a mature epithelial layer (indicated by green tracking). After this period, fibrillated microrods were biofabricated atop the previously constructed GelMA membranes, which contained encapsulated PRs at a concentration of 1 million cells mL derived from dissociated retinal organoids. The cell-loaded Janus Assembly was then maintained in culture and monitored over a span of 7 days.

Cell Culture—HDF and C2C12: HDFs were cultured in Dulbecco's Modified Eagle Medium supplemented with GlutaMAX (Gibco), 10% fetal bovine serum (Gibco), and 1% penicillin-streptomycin (Gibco) at 37 °C in a humidified atmosphere with 5% CO_2. Once the cells reached confluency, they were trypsinized using TrypLE (Gibco) for use in subsequent experiments. Similar protocols were employed for C2C12 cells.

Cell Culture—Human IPSCS and IECS Culture: iECs were generously provided by our collaborator at Cedars-Sinai Biomanufacturing Center. The iEC differentiation methodology has been previously documented.[49] In brief, undifferentiated iPSCs, originally reprogrammed from healthy donor peripheral blood mononuclear cells (PBMCs) were seeded and cultured in mTeSR+ medium (STEMCELL Technologies) on recombinant human laminin 521 (BioLamina)-coated plates. The differentiation of iECs from iPSCs was conducted over three distinct phases. During phase 1, iPSCs were induced toward mesodermal lineage using CHIR99021 (Xcess Bio) for a period of 2 days. Subsequently, vascular progenitors were generated through treatment with a combination of bone morphogenic protein 4 (BMP4; R&D Systems), fibroblast growth factor 2 (FGF2; PeproTech), and vascular endothelial growth factor (VEGF165; PeproTech) in STEMd-iffAPEL2 (STEMCELL Technologies) for an additional 2 days during phase 2. Finally, iECs were replated onto recombinant laminin 421 (BioLamina)-coated plates and cultured in EC growth medium MV2 (ECGM-MV2; PromoCell) supplemented with VEGF165 to facilitate endothelial cell induction over a period of 7 days, with media changes performed every other day.

Stem Cells and RPE Differentiation: The differentiation of H9 human embryonic stem cells (hESCs) into RPE cells and the generation of retinal organoids entail several crucial steps. The hESCs, sourced from Wi-Cell (Madison), were initially cultured in mTeSR1 medium supplied by STEMCELL Technologies. Over a period of 12 weeks, these cells underwent differentiation into RPE cells in the XVIVO 10 medium (Lonza).[50] The pigmented RPE-like cells that developed were enriched through mechanical isolation. Following isolation, these cells underwent further processing, including dissociation with TrypLE (Life Technologies) and subsequent culture on plates coated with human vitronectin (AMS Biotechnology) in XVIVO 10 medium. Cells at passage 3 were then prepared for additional experiments.[50]

To generate retinal organoids, hESCs were genetically modified to express a green fluorescent protein (GFP) tagged CRX gene, a generous contribution from Majlinda Lako at Newcastle University, UK. The CRX-GFP cells, derived from H9 (NIH 0043), were cultured at the University of Southern California (USC, Los Angeles, CA) under a material transfer agreement with the University of Newcastle's Biosciences Institute. The CRX gene encodes the cone-rod homeobox protein, specifically expressed in photoreceptor cells. The CRX-GFP H9 cells were maintained in mTeSR1 medium (STEMCELL Technologies) and passaged at 80% confluency using ReLeSR (STEMCELL Technologies). These media and supplements were selected for their effectiveness in supporting cell growth and differentiation. Cells were expanded on plates coated with BD GFR Matrigel and incubated in a humidified atmosphere of 95% oxygen, 5% CO_2, and 37 °C.

When cultures became confluent, they were dissociated into single cells using Accutase (Nacalai Inc) to initiate retinal organoid differentiation. The cells were then transferred to 800-µm micro-well EZSPHERE 6-well plates and centrifuged at 100 g for 3 min, allowing embryoid bodies (EBs) to form over the first 7 days. On day 8, the EBs were transferred to culture dishes coated with 1% growth factor-reduced Matrigel (Corning). The medium was gradually shifted from mTeSR1 to neural induction media (NIM) containing DMEM/F12 (1:1) (Gibco), 1% N2 supplement (Gibco), 1x nonessential amino acids (NEAA) (Gibco), 1x L-glutamine (Gibco), and 2 µg mL^{-1} heparin (Sigma–Aldrich), with daily media changes. These formulations were selected for their capacity to induce neural differentiation. The EBs adhered and began differentiating into eye field structures. From days 19 to 41, the media was switched to NIM supplemented with 2% B27 supplement (minus vitamin A, Gibco), 1x NEAA, 1x L-glutamine, and 2 mg mL^{-1} heparin (Sigma). These supplements were chosen to enhance cell survival and growth. Between days 40 and 50, retinal eye fields were manually dissected from the dish and transferred to ultralow attachment 24-well plates (Corning). From day 42 onward, the organoids were cultured in DMEM/F12 (1:1) with 10% FBS, supplemented with 2% B27 Plus Supplement (Gibco), 1x NEAA, 1x L-glutamine, 2 µg/ml heparin, and 100 µM taurine (Sigma).

Dissociation of Retinal Organoids: To dissociate the retinal organoids, advanced equipment and techniques were utilized. A papain solution (10 mg mL^{-1}) was prepared by diluting 1:100 in an activation buffer and incubated in an open tube in a cell culture incubator set to 7% CO_2 for 30 min to activate the enzyme. The organoids were collected into a tube and washed with Hanks' Balanced Salt Solution (HBSS) prior to digestion. For dissociation, the organoids were incubated at 37 °C with the activated papain solution for 15 min, with agitation every two min. The organoids were then pipetted to resuspend the cell clusters, washed with OC media, and strained through a 0.4-µm cell strainer.

Cell viability, Proliferation, and Cytoskeleton Staining: Cell viability was assessed using calcein AM (1 µM, Invitrogen) and ethidium homodimer (1 µM, Invitrogen) staining at room temperature for 20 min. Following staining, the samples were washed with 1X DPBS and visualized using confocal microscopy (Zeiss LSM 700) at 488 nm for calcein AM (green, indicating viable cells) and 561 nm for ethidium homodimer (red, indicating dead cells).

Cell proliferation was quantified using PrestoBlue cell viability reagent at various time points. Briefly, a working solution of PrestoBlue (Invitrogen) was prepared by diluting it 1:10 with complete media according to the manufacturer's protocol. The complete media was removed from the samples, and PrestoBlue solution was added before incubating for 3 h at 37 °C in a 5% CO_2 incubator. After incubation, the solution was collected from each sample, and absorbance was measured at 570 and 600 nm using a Varioskan Lux plate reader (Thermo Fisher Scientific). The cell proliferation rate, which was directly proportional to the percentage of dye reduction, was calculated from the absorbance data and presented as a bar graph with standard deviations, using triplicate samples for each time point.

Cell morphology was examined through actin staining. At specified time points, cells were fixed overnight at 4 °C with 4% formaldehyde solution, then washed with 1X DPBS and treated with 0.1% Triton X-100 for 10 min. These permeabilized samples were washed three times with 1X DPBS and blocked with 1% bovine serum albumin for 30 min, followed by additional washing with 1X DPBS. Alexa Fluor 594 phalloidin (Invitrogen) was then added for a 30-min incubation at room temperature. The fluorescently stained microgels were washed with 1X DPBS, and the nuclei were stained with DAPI (Invitrogen) for 5 min. Finally, the fluorescently stained microgels were imaged using confocal microscopy (Zeiss LSM 700) for the fluorescent channels at 594 nm (cytoskeleton, red) and 405 nm (nuclei, blue).

IF Staining: For C2C12 staining, microrods loaded with cells were fixed for 20 min in a 4% paraformaldehyde solution after 4 days of culture in the differentiation media. This fixation was followed by a 10-min permeabilization step using Triton X-100 and a 30-min blocking step with a 1% BSA solution. The blocked samples were then incubated overnight at 4 °C with the primary antibody Anti-Desmin [ab15200, Abcam] to assess the formation of heavy chain myotubes. After overnight incubation, the samples were treated with a secondary antibody (Goat Anti-rabbit Alexa Fluor 488, Abcam) for 1 h. Following this incubation, the samples were washed three times with PBS, counterstained with DAPI, and observed under a confocal microscope. For Myosin Heavy Chain staining (MYHC) similar protocol was adopted at 7 days post-induction in differentiation media.

**ADVANCED
SCIENCE NEWS**

www.advancedsciencenews.com

NANO · MICRO
small

www.small-journal.com

The primary antibody used was anti-myosin (MYH, ab37484, host species mouse). A secondary antibody was selected based on the primary (Rabbit anti-mouse, Alexa Fluor 488, Invitrogen).

For staining of CD31, Recoverin, and ZO-1 in modular assemblies, a similar procedure was followed. The primary antibodies used included Rabbit polyclonal to CD31 (ab28364, Abcam), Rabbit polyclonal Recoverin antibody (6a55cd6, Abcam), and ZO-1 Monoclonal Antibody (ZO1-1A12, Abcam) for CD31, Recoverin, and ZO-1, respectively. The secondary antibodies were selected based on the source of the primary antibodies.

Subcutaneous Implantation: All surgeries were conducted in an aesthetic environment, adhering to standard ethical protocols. Briefly, male C57Bl/6 mice aged 6 months were anesthetized with isoflurane vapors. The mouse abdomen was sterilized with 70% isopropyl alcohol, and two 200 µL plugs were injected into the abdomen using a 21G syringe and forceps. A total of 4 animals were used for each injection, with two plugs injected into each animal (left and right cavities), resulting in 8 subcutaneous injections per shape across the four animals. Following microgel plugs were injected: 1. Rod-shaped microgels, 2. Rod-shaped microgels with QK peptide, 3. Square-shaped microgels, and 4. Square-shaped microgels with QK peptide. After 2 weeks, the animals were euthanized, and the tissue plugs were isolated and embedded in OCT for cryosectioning. Hematoxylin and eosin (H&E) staining was performed on the cryosections from the isolated plugs to assess tissue infiltration, and sections were also stained for CD31 to evaluate neovascularization following standard protocols.

Statistical Analysis: Quantitative variables were evaluated for normality using statistical tests such as Shapiro-Wilk or Kolmogorov-Smirnov, along with descriptive statistics and graphical analyses, including QQ plots. For parametric data, analysis of variance (ANOVA, one-way or two-way) was conducted, followed by Tukey's post hoc test to assess differences between groups and time points in both in vitro and in vivo experiments. Unpaired t-tests were used for comparisons involving two groups. Nonparametric data were analyzed using the Kruskal–Wallis test to examine differences between groups and time points. For nonparametric comparisons between two groups, the Mann–Whitney test was applied for unpaired samples. Statistical significance was set at $p < 0.05$, with significance levels indicated by asterisks (* $p < 0.05$, ** $p < 0.01$, *** $p < 0.001$, **** $p < 0.0001$). All statistical analyses were performed using GraphPad Prism version 9 for Windows.

Disclaimers: The funders were not involved in the study design, collection, analysis, interpretation of data, the writing of this article, or the decision to submit it for publication. The data and views expressed in this article were those of the authors and may not reflect the official policy or position of the Department of the Army, Department of Defense, or the US Government.

Ethical Approvals: Human cell lines were obtained or created at Cedars-Sinai under the auspices of the Cedars-Sinai Medical Center Institutional Review Board (IRB)-approved protocols. Specifically, the iPSC cell lines and differentiation protocols in the present study were carried out in accordance with the guidelines approved by the Stem Cell Research Oversight (SCRO) committee and IRB, under the auspices of IRB-SCRO Protocols Pro00032834 (iPSC Core Repository and Stem Cell Program), Pro00036896 (Sareen Stem Cell Program) and STUDY00001019: MTEC Qual-Regen. In vitro studies using human cell lines were conducted from participants who provided written informed consent for research studies.

Supporting Information

Supporting Information is available from the Wiley Online Library or from the author.

Acknowledgements

Conflict of Interest

The authors declare no conflict of interest.

Data Availability Statement

The data that support the findings of this study are available from the corresponding author upon reasonable request.

Keywords

[1] H. Simaan-Yameen, O. Bar-Am, G. Saar, D. Seliktar, *Acta Biomater.* **2023**, *164*, 94.

[2] T. Arndt, U. Chatterjee, O. Shilkova, J. Francis, J. Lundkvist, D. Johansson, B. Schmuck, G. Greco, Å. E. Nordberg, Y. Li, *Adv. Funct. Mater.* **2023**, *34*, 2303622.

[3] C. Ma, X. Duan, X. Lei, *Front. Bioeng. Biotechnol.* **2023**, *11*, 1136583.

[4] T. Su, M. Zhang, Q. Zeng, W. Pan, Y. Huang, Y. Qian, W. Dong, X. Qi, J. Shen, *Bioact. Mater.* **2021**, *6*, 579.

[5] L. Lian, M. Xie, Z. Luo, Z. Zhang, S. Maharjan, X. Mu, C. E. Garciamendez-Mijares, X. Kuang, J. K. Sahoo, G. Tang, *Adv. Mater.* **2024**, *36*, 2304846.

[6] H. Kim, B. Kang, X. Cui, S. H. Lee, K. Lee, D. W. Cho, W. Hwang, T. B. Woodfield, K. S. Lim, J. Jang, *Adv. Funct. Mater.* **2021**, *31*, 2011252.

[7] L. Hao, H. Mao, *Biomater. Sci.* **2023**, *11*, 6384.

[8] N. Pien, H. Krzyslak, S. S. Kallaje, J. Van Meerssche, D. Mantovani, C. De Schauwer, P. Dubruel, S. Van Vlierberghe, C. Pennisi, *Appl. Mater. Today* **2023**, *31*, 101737.

[9] W-H. Huang, S-L. Ding, X-Y. Zhao, K. Li, H-T. Guo, M-Z. Zhang, Q. Gu, *Mater. Today Bio.* **2023**, *20*, 100639.

[10] J. Sapudom, S. Karaman, B. C. Quartey, W. K. E. Mohamed, N. Mahtani, A. Garcia-Sabaté, J. Teo, *Adv. Sci.* **2023**, *10*, 2301353.

[11] M. J. Shin, S. H. Im, B. Kim, J. Choi, S. E. Lucia, W. Kim, J. G. Park, P. Kim, H. J. Chung, D. K. Yoon, *ACS Appl. Mater. Interfaces* **2023**, *15*, 18653.

ADVANCED
SCIENCE NEWS

www.advancedsciencenews.com

NANO · MICRO
small

www.small-journal.com

[12] L. V. Le, M. A. Mkrtschjan, B. Russell, T. A. Desai, *Biomed. Microdevices* **2019**, *21*, 43.

[13] I. Jorba, S. Gussenhoven, A. van der Pol, B. G. Groenen, M. van Zon, M. J. Goumans, N. A. Kurniawan, T. Ristori, C. V. Bouten, *Biofabrication* **2024**, *16*, 035011.

[14] M. Lewis, G. David, D. Jacobs, P. Kuczwara, A. E. Woessner, J-W. Kim, K. P. Quinn, Y. Song, *Mater. Today Bio.* **2023**, *22*, 100762.

[15] H. Park, S. N. Nazhat, D. H. Rosenzweig, *Biomaterials* **2022**, *286*, 121606.

[16] A. Ahmed, I. M. Joshi, M. Mansouri, N. N. Ahamed, M-C. Hsu, T. R. Gaborski, V. V. Abhyankar, *Am. J. Physiol.: Cell Physiol.* **2021**, *320*, C1112.

[17] M. E. Prendergast, M. D. Davidson, J. A. Burdick, *Biofabrication* **2021**, *13*, 044108.

[18] A. L. Castro, S. Vedaraman, T. Haraszti, M. A. Barbosa, R. M. Gonçalves, L. De Laporte, *Adv. Mater. Technol.* **2024**, *9*, 2301391.

[19] W. Chen, Z. Zhang, P. H. Kouwer, *Small* **2022**, *18*, 2203033.

[20] T. H. Qazi, J. Wu, V. G. Muir, S. Weintraub, S. E. Gullbrand, D. Lee, D. Issadore, J. A. Burdick, *Adv. Mater.* **2022**, *34*, 2109194.

[21] D. Rommel, M. Mork, S. Vedaraman, C. Bastard, L. P. Guerzoni, Y. Kittel, R. Vinokur, N. Born, T. Haraszti, L. De Laporte, *Adv. Sci.* **2022**, *9*, 2103554.

[22] Q. Feng, D. Li, Q. Li, X. Cao, H. Dong, *Bioact. Mater.* **2022**, *9*, 105.

[23] S. Saxena, C. E. Hansen, L. A. Lyon, *Acc. Chem. Res.* **2014**, *47*, 2426.

[24] H. Shieh, M. Saadatmand, M. Eskandari, D. Bastani, *Sci. Rep.* **2021**, *11*, 1565.

[25] N. Weigel, Y. Li, J. Thiele, A. Fery, *Curr. Opin. Colloid Interface Sci.* **2023**, *64*, 101673.

[26] Q. Wang, Ö. Karadas, O. Backman, L. Wang, T. Näreoja, J. M. Rosenholm, C. Xu, X. Wang, *Adv. Healthcare Mater.* **2023**, *12*, 2203243.

[27] V. G. Muir, S. Weintraub, A. P. Dhand, H. Fallahi, L. Han, J. A. Burdick, *Adv. Sci.* **2023**, *10*, 2206117.

[28] B. E. Kelly, I. Bhattacharya, H. Heidari, M. Shusteff, C. M. Spadaccini, H. K. Taylor, *Science* **2019**, *363*, 1075.

[29] P. N. Bernal, P. Delrot, D. Loterie, Y. Li, J. Malda, C. Moser, R. Levato, *Adv. Mater.* **2019**, *31*, 1904209.

[30] H. Liu, P. Chansoria, P. Delrot, E. Angelidakis, R. Rizzo, D. Rütsche, L. A. Applegate, D. Loterie, M. Zenobi-Wong, F. Light, *Adv. Mater.* **2022**, *34*, 2204301.

[31] P. Chansoria, R. Rizzo, D. Rütsche, H. Liu, P. Delrot, M. Zenobi-Wong, *Chem. Rev.* **2024**, *124*, 8787.

[32] A. Puiggalí-Jou, R. Rizzo, A. Bonato, P. Fisch, S. Ponta, D. M. Weber, M. Zenobi-Wong, *Adv. Healthcare Mater.* **2024**, *13*, 2302179.

[33] C. M. Franca, A. Athirasala, R. Subbiah, A. Tahayeri, P. Selvakumar, A. Mansoorifar, S. Horsophonphong, A. Sercia, L. Nih, L. E. Bertassoni, *Adv. Healthcare Mater.* **2023**, *12*, 2202840.

[34] R. Goodrich, Y. Tai, Z. Ye, Y. Yin, J. Nam, *Adv. Funct. Mater.* **2023**, *33*, 2211288.

[35] A. Pardo, M. Gomez-Florit, M. D. Davidson, M. Özgen Öztürk-Öncel, R. M. Domingues, J. A. Burdick, M. E. Gomes, *Adv. Healthcare Mater.* **2024**, *13*, 2303167.

[36] R. Dubay, J. N. Urban, E. M. Darling, *Adv. Funct. Mater.* **2021**, *31*, 2009946.

[37] Y. Kittel, A. J. Kuehne, L. De Laporte, *Adv. Healthcare Mater.* **2022**, *11*, 2101989.

[38] R. Lev, O. Bar-Am, G. Saar, O. Guardiola, G. Minchiotti, E. Peled, D. Seliktar, *Cell Death Dis.* **2024**, *15*, 470.

[39] Y. Wang, R. K. Kankala, Y-Y. Cai, H-X. Tang, K. Zhu, J-T. Zhang, D-Y. Yang, S-B. Wang, Y. S. Zhang, A-Z. Chen, *Biomaterials* **2021**, *277*, 121072.

[40] R. S. Molday, O. L. Moritz, *J. Cell Sci.* **2015**, *128*, 4039.

[41] D. Muller, H. Chim, A. Bader, M. Whiteman, J-T. Schantz, *Stem Cells Int.* **2011**, *2011*, 547247.

[42] P. Xia, Y. Luo, *J. Biomed. Mater. Res., Part B* **2022**, *110*, 1206.

[43] Q. Liu, J. Xie, R. Zhou, J. Deng, W. Nie, S. Sun, H. Wang, C. Shi, *Neural Regener. Res.* **2025**, *20*, 503.

[44] W. Xu, Y. Wu, H. Lu, X. Zhang, Y. Zhu, S. Liu, Z. Zhang, J. Ye, W. Yang, *Acta Biomater.* **2023**, *160*, 225.

[45] P. N. Bernal, M. Bouwmeester, J. Madrid-Wolff, M. Falandt, S. Florczak, N. G. Rodriguez, Y. Li, G. Größbacher, R. A. Samsom, M. van Wolferen, *Adv. Mater.* **2022**, *3*, 2110054.

[46] A. Joshi, T. Kaur, A. Joshi, S. B. Gugulothu, S. Choudhury, N. Singh, *ACS Appl. Mater. Interfaces* **2022**, *15*, 327.

[47] N. Moghimi, M. Kamaraj, F. Zehtabi, S. A. Yavari, M. Kohandel, A. Khademhosseini, J. V. John, *J. Mater. Chem. B* **2024**, *12*, 2818.

[48] J. M. Zatorski, A. N. Montalbine, J. E. Ortiz-Cárdenas, R. R. Pompano, *Anal. Bioanal. Chem.* **2020**, *412*, 6211.

[49] N. R. Ariyasinghe, R. de Souza Santos, A. Gross, A. Aghamaleky-Sarvestany, S. Kreimer, S. Escopete, S. J. Parker, D. Sareen, *Physiol. Genomics* **2023**, *55*, 324.

[50] B. Diniz, P. Thomas, B. Thomas, R. Ribeiro, Y. Hu, R. Brant, A. Ahuja, D. Zhu, L. Liu, M. Koss, *Invest. Ophthalmol. Visual Sci.* **2013**, *54*, 5087.